



**Linking surface chemistry to photovoltage in Sr-substituted
LaFeO₃ for water oxidation**

Journal:	<i>Journal of Materials Chemistry A</i>
Manuscript ID	TA-ART-06-2018-005741.R1
Article Type:	Paper
Date Submitted by the Author:	06-Aug-2018
Complete List of Authors:	<p>Stoerzinger, Kelsey; Pacific Northwest National Laboratory, Physical and Computational Sciences Directorate Wang, Le; Pacific Northwest National Laboratory, Physical and Computational Sciences Directorate Ye, Yifan; Lawrence Berkeley National Laboratory, Chemical Sciences Division Bowden, Mark; Pacific Northwest National laboratory, Environmental Molecular Sciences Laboratory Crumlin, Ethan; Lawrence Berkeley National Laboratory, Advanced Light Srouce Du, Yingge; Pacific Northwest National Laboratory, Physical and Computational Sciences Directorate Chambers, Scott; Pacific Northwest National laboratory, Physical and Computational Sciences Directorate</p>

Linking surface chemistry to photovoltage in Sr-substituted LaFeO₃ for water oxidationKelsey A. Stoerzinger,^{1,*} Le Wang,¹ Yifan Ye,² Mark Bowden,³ Ethan J. Crumlin,⁴ Yingge Du,¹Scott A. Chambers¹¹*Physical and Computational Sciences Directorate, Pacific Northwest National Laboratory, 902**Battelle Blvd, Richland WA 99352, USA*²*Chemical Sciences Division, Lawrence Berkeley National Laboratory, 1 Cyclotron Road**Berkeley CA 94720, USA*³*Environmental Molecular Sciences Laboratory, Pacific Northwest National Laboratory,**Richland WA 99352, USA*⁴*Advanced Light Source, Lawrence Berkeley National Laboratory, 1 Cyclotron Road**Berkeley CA 94720, USA*

*kelsey.stoerzinger@pnl.gov

Abstract: Perovskite oxides are promising materials for photoabsorbers and electrocatalysts for solar-driven water oxidation. Aliovalent doping can tune the transition metal redox properties as well as the material band gap and conductivity, resulting in a rich phase space of possible water-oxidation photoanodes. We consider the substitution of Sr²⁺ for La³⁺ in LaFeO₃ epitaxial thin films, where the well-defined nature of the flat surface and path for charge transport enables fundamental studies of photoelectrochemical (PEC) water oxidation. Sr incorporation increases the photovoltage, but at the expense of photocurrent. The use of a fast redox couple to efficiently collect photogenerated holes indicates an even lower onset of oxidative current; the difference between this onset and that of water oxidation arises from the involvement of surface states during water oxidation. Measurements of the surface speciation in a humid environment demonstrate that Sr incorporation also promotes hydroxylation, suggesting that water oxidation

proceeds through the oxidation of Fe^{III}-OH states, which is facilitated by Sr incorporation and results in an increased photovoltage.

Introduction:

The direct collection and storage of solar energy through photoelectrochemical (PEC) water splitting is a promising route to the renewable generation of hydrogen fuel. Semiconducting photoelectrodes can be used to absorb light, separate photogenerated charge carriers, and in some cases, perform catalysis.¹ The material requirements are extensive—resulting in a decades-long search since the first seminal report²—including stability, high efficiency, and low cost from earth-abundant elements.³ For the water-oxidizing photoanode, much work has focused on hematite (α -Fe₂O₃) on account of its band gap within the visible, the ability of photogenerated holes to evolve O₂ gas due to the band level alignment, and the elemental abundance of Fe.⁴ However, a significant overpotential is still required to oxidize water, with little known about the mechanism at oxide electrodes, and numerous open questions regarding the design of more efficient photoanodes to enable solar hydrogen production.

Extensive studies have been performed on Fe₂O₃ to elucidate the limiting material parameters, reaction mechanism, and ultimately design more active photoanodes. Studies with fast redox shuttles coupled with in situ infrared spectroscopy have shown that photogenerated holes initially oxidize the electrode surface under water oxidation conditions, attributed to the first step in water oxidation.^{5, 6} The requirement to “charge” these surface states at a given potential then reduces the photovoltage obtained during photoelectrochemical (PEC) water splitting, though some controversy remains with respect to the role of in-gap states and the reaction mechanism.^{4, 7} The photocurrent can be limited by recombination of charge carriers

before reaching the electrolyte interface, resulting from the low hole mobility of transition metal oxides.⁸ One mitigation strategy is to increase conductivity by doping, which can increase the carrier concentration and diffusion length.⁹ In addition, substitution at higher concentrations can lead to changes in the material Fermi level,¹⁰ or in some cases band gap, then impacting the photovoltage as well.

Complex oxides, such as in the ABO_3 perovskite crystal structure, offer additional parameters to tune and manipulate electronic structure.¹¹ Maintaining the abundant and benign element of Fe, $LaFeO_3$ (LFO) has demonstrated promising photocatalytic performance in sacrificial donor-assisted water splitting and dye degradation.¹²⁻¹⁴ The band gap is ~ 2.3 eV¹⁵ with a valence band sufficiently low to oxidize water,¹⁶ and ferrites can have reasonable catalytic activity for oxygen evolution.¹⁷⁻¹⁹ A recent report has demonstrated unassisted PEC water splitting on LFO,²⁰ as its conduction band also spans the hydrogen redox potential, further motivating fundamental studies of its electronic structure to improve absorption and charge transport. However, the obtained photovoltage and photocurrent for LFO during the oxygen evolution reaction (OER) is low.²¹ Hybrid density functional theory studies of LFO have recently shown that electronic charges localize as small hole and electron polarons (similar to Fe_2O_3)²² leading to low mobility. Similar to studies of binary oxides, the PEC activity of LFO can be improved by B-site (Fe) doping.^{23, 24} Of further promise is the fact that Sr substitution on the A-site (La) acts as an acceptor and enables electronic conductivity through hole polarons²² in addition to narrowing the band gap.²⁵ Lacking, however, is an understanding of how Sr substitution influences the surface electronic structure, chemical speciation, band bending, and ultimately PEC activity.

In this work, we have studied the role of A-site doping in $\text{La}_{(1-x)}\text{Sr}_x\text{FeO}_3$ (LSFO) epitaxial films on the electronic states and chemical species at the electrode/electrolyte interface, as well as the resultant photovoltage and photocurrent for water oxidation. Thin films serve as excellent models for nanostructured PEC systems since the charge collection dimensions can be controlled by film thickness²⁶ and epitaxial films can disentangle intrinsic transport properties without convolution from morphological or crystalline structural defects.⁹ We find that Sr-substitution increases the photovoltage obtained from wavelength-selected light sources, being negligible for LaFeO_3 (LFO) under 460 nm blue LED illumination but >0.5 V for $\text{La}_{0.8}\text{Sr}_{0.2}\text{FeO}_{3-\delta}$ (Sr20), though at a cost to photocurrent compared to $\text{La}_{0.88}\text{Sr}_{0.12}\text{FeO}_{3-\delta}$ (Sr12). Measurements with the fast redox shuttle $[\text{Fe}(\text{CN})_6]^{3-/4-}$ indicate that water oxidation proceeds through the accumulation of photogenerated holes, located at lower potentials on the reversible hydrogen electrode (RHE) scale for Sr20. Probing the surface oxygen speciation in a humid environment with ambient pressure X-ray photoelectron spectroscopy (AP-XPS) indicates that any oxygen vacancies present are filled by hydroxyls, and that Sr20 has a higher affinity to dissociate water. These findings suggest that aliovalent doping of a non-redox active metal (i.e. Sr) in perovskite oxides can facilitate the formation of surface reaction intermediates (such as OH) and their oxidation at the redox active site (Fe), thus enhancing the photovoltage.

Experimental methods:

Film growth. 30 nm LSFO ($x=0, 0.12, 0.2$) films were grown on (001)-oriented 0.1 wt% Nb-doped SrTiO_3 (Nb:STO) (Crystec) by oxygen assisted pulsed laser deposition (OA-PLD) for PEC studies.²⁷ Laser pulses ($\lambda = 248$ nm) of energy density equal to ~ 2 J-cm⁻² and a repetition rate of 1 Hz were programmed to be incident on LaFeO_3 and SrFeO_3 targets with different pulse

ratios to achieve the desired composition. The substrate temperature was 700 °C. The growth oxygen pressure was 10 mTorr and the growth rate was about 1 nm (2.5 u.c.) /min. After growth, the samples were cooled down to room temperature in 10 mTorr oxygen.

Films for AP-XPS and X-ray absorption spectroscopy (XAS) were grown by oxygen plasma assisted molecular beam epitaxy (OPA-MBE).²⁸ 30 nm LFO and Sr20 films and 9 u.c. Sr12 films were grown on 0.1 wt% Nb:STO (Crystec). The substrate was held at 650 °C, and high-purity Sr, La and Fe were co-evaporated from effusion cells in activated oxygen from an electron cyclotron plasma source at a partial pressure of 2×10^{-6} Torr. Typical growth rates were ~1.3 unit cells (u.c.)/min. The individual metal fluxes were established using a quartz crystal oscillator placed at the substrate position prior to film growth.

Film characterization. *In situ* reflection high-energy electron diffraction (RHEED) was used to monitor the surface quality and growth rate during MBE deposition. Crystal structures were determined using high-resolution X-ray diffraction (XRD) with a Philips X'Pert four-circle diffractometer (**Figure S1**). The surface morphology of the LSFO films was examined using an atomic force microscope (AFM) (**Figure S2**). Spectroscopic ellipsometry measurements were performed using a rotating analyzer instrument with compensator (V-VASE; J.A. Woollam Co., Inc.) over the spectral range from 0.36 to 4.76 eV. Data was collected at three different incidence angles automatically: 65°, 70° and 75°. To extract physically reasonable optical functions (n and k), a simple two-layer model (film/substrate) was used.

Electrochemistry. Films were contacted by scratching a GaIn eutectic (Sigma, >99.99%) into the back of the Nb:STO substrate, and a Cu wire held in contact with the pad in a custom-built compression cell. The 0.1 M KOH electrolyte was prepared from Nanopure water (18.2 MΩ-cm) and KOH pellets (Sigma Aldrich, 99.99%), and saturated with ultra-high purity O₂ gas

to fix the equilibrium potential. Measurements were made with a Biologic SP-200 potentiostat, and voltages corrected for the electrolyte resistance between the working and reference electrodes from the high frequency intercept of electrochemical impedance. The saturated calomel reference electrode (RE-2BP, ALS Co.) was calibrated to the reversible hydrogen electrode (RHE) scale in the same electrolyte, saturated with H₂ and using Pt working and counter electrodes. A Pt counter electrode (ALS Co.) was also used for PEC measurements.

Light from ultra-high power LEDs (Prizmatix) was incident through a planar quartz window. The illuminated area of the sample was defined by the PEEK holder, and was commensurate with the area exposed to the electrolyte. The intensity of the LED at the location of the sample was measured after passing through the quartz window with a Newport 843-R power meter, and estimated to attenuate ~5% (520 nm, 460 nm) or ~10% (630 nm) over the ~6 cm path length from water absorption.

For fast redox (FeCN) and surface state (KOH only) measurements, GaIn eutectic (Sigma, >99.99%) was scratched into the back of the Nb:STO substrate, and a Cu wire held in contact with this GaIn pad using Ag paste (Liebsilber, Ted Pella). The wire contact, back and sides of the electrode were covered with inert epoxy (Loctite 9460) such that only the LSFO surface was exposed to the electrolyte. This enabled the film to be held closer to the quartz window for greater illumination. The FeCN electrolyte was prepared by adding 5 mM each of K₃Fe(CN)₆ and K₄Fe(CN)₆·3H₂O (Sigma, >99%) to the 0.1 M KOH electrolyte, and the electrolyte was saturated with ultra-high purity N₂ with a Ag/AgCl reference electrode (ALS Co.) calibrated to the RHE.

Ambient-Pressure X-ray Photoelectron Spectroscopy (AP-XPS). AP-XPS was collected at Beamline 9.3.2²⁹ at Lawrence Berkeley National Laboratory's (LBNL) Advanced

Light Source (ALS). Films were placed onto a ceramic heater. A thermocouple was pressed into a gold foil mounted directly onto the sample surface for temperature measurements, and isolated from the sample holder clips with an Al₂O₃ spacer. The binding energy scale was initially calibrated using the Au 4f (84 eV). Subsequent spectra were aligned using either the O 1s bulk feature (for 690 eV incident photon energy, IPE) or La 4d (350 eV IPE) as an internal reference. Negligible beam-induced changes were observed, probed by comparing the O 1s at an irradiated spot to a fresh spot that had not been exposed to the X-ray beam prior to a quick acquisition (**Figure S3**).

The samples were cleaned by heating to 300 °C in $p(\text{O}_2)$ of 100 mTorr (measured by a calibrated capacitance gauge) until clean of carbon. After characterization of the clean surface in O₂, varying pressure of H₂O was introduced on top of the stable O₂ pressure. The H₂O was prepared from deionized water (Millipore, >18.2 MΩ cm) and degassed by several freeze-pump-thaw cycles. For the annealed Sr12 film, the sample was first cleaned at 300 °C in O₂, then evacuated to $\sim 1 \times 10^{-7}$ Torr. The temperature was ramped in UHV from 300 to 600 °C over the course of an hour, then held at 600 °C for ~ 25 minutes. The sample was then cooled over 40 minutes to reach 300 °C with a base pressure of 2×10^{-8} Torr. After characterization, $p(\text{H}_2\text{O})$ was increased starting at 10 mTorr. Valence band spectra were smoothed by adjacent averaging over five points, which did not influence the location of any features.

O 1s spectra were deconvolved with Gaussian–Lorentzian (GL) peaks using CasaXPS after a Shirley-type background subtraction (**Table S1**). The O 1s integrated area of the (bi)carbonate peak was calculated from the area of the C 1s (bi)carbonate peak using an O 1s:C 1s relative sensitivity factor, which was experimentally calibrated using the core levels of CO₂ gas.³⁰

Near Edge X-ray Absorption Fine Structure (NEXAFS). NEXAFS was also collected at Beamline 9.3.2 at LBNL's ALS. Spectra were collected between AP-XPS measurements at 300 °C in O₂ and H₂O. The detector was set to collect 40 eV kinetic energy photoelectrons. A linear pre-edge was subtracted from the spectra, which were subsequently normalized to the post-edge and smoothed by adjacent averaging over five points, which did not influence the location of any features. The location of the O K pre-edge for an LaFeO₃ reference¹⁶ was used to calibrate the energy scale.

Results and Discussion:

High quality LSFO thin films (LFO, Sr12, Sr20) were grown on (001)-oriented Nb:STO substrates and the epitaxial relationship (LSFO [100](001) // STO[100](001)) confirmed by XRD (**Figure S1**). AFM images (**Figure S2**) for the LSFO films show evenly spaced surface steps, revealing an atomically smooth surface. Compared to LFO, the substitution of Sr²⁺ for La³⁺ leads to nominal oxidation of the Fe and/or some incorporation of oxygen vacancies. In addition to increasing film conductivity,³¹ Sr incorporation reduces the optical gap, measured by spectroscopic ellipsometry (**Figure 1 a**). Similar trends have been observed by others.^{25,32}

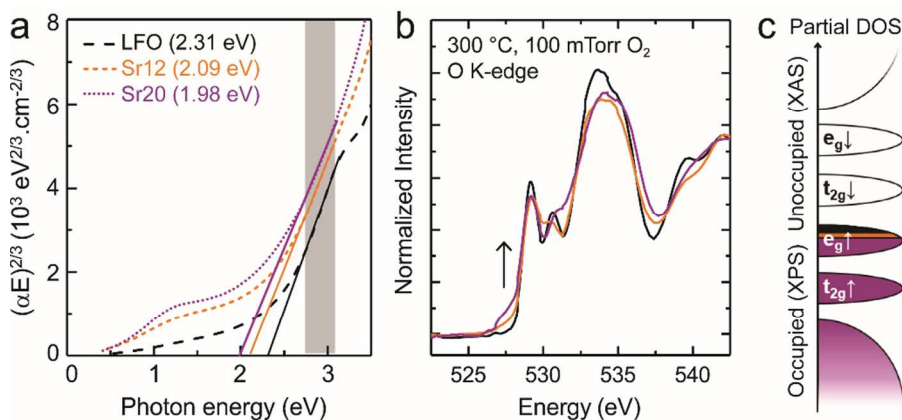


Fig 1. (a) Spectroscopic ellipsometry measurements for LSFO films LFO (black), Sr12 (dashed orange), and Sr20 (dotted purple). Fits to the linear shaded region of the Tauc plot yield the noted band gap, obtained by the intercept, modelling inter-band optical transitions as direct, dipole-forbidden excitations.¹⁵ (b) O K-edge measured at 300 °C in 100 mTorr O₂ (dry, oxidizing conditions) for cleaned films with corresponding color to (a). A pre-edge feature at lower energies (527.5 eV) increases with Sr incorporation and Fe oxidation. (c) Schematic of the partial density of states (DOS) in the oxide band structure. The e_g^\uparrow band is filled for LFO, but becomes partially unoccupied with Sr doping.

To better understand the changes in electronic structure resulting from Sr incorporation, XAS was performed at the O K-edge (**Figure 1 b**). The films were characterized at 300 °C in a background pressure of 100 mTorr O₂ to maintain a clean surface at similar oxygen chemical potentials to growth conditions. The incorporation of Sr leads to an increase in intensity at energies below the e_g and t_{2g} features³³ of the pre-edge (at 529-531 eV), indicating new unoccupied states of mixed O 2p and Fe 3d character. In parallel, there is a decrease in occupied states at the top of the valence band (**Figure S4**), coupled with a small shift in the valence band edge toward the Fermi level. These findings are consistent with studies of polaronic transport in LSFO³⁴ and previous XAS studies in UHV.^{35, 36} Thus Sr incorporation transfers weight from the top of the valence band to the bottom of the conduction band, and the reduction in band gap arises from new transitions to these lower energy covalent states.

Motivated by the reduction in band gap through a lowering of the conduction band edge, we investigate the performance of LSFO thin films as model photoanodes for water oxidation in 0.1 M KOH. The layer-by-layer growth on single crystal (001)-oriented substrates results in a

smooth, planar surface, and a measure of intrinsic activity when normalized to the oxide surface area. However, the resultant high reflectivity and low surface area does result in low current densities, which would be improved with nanostructuring. LFO exhibits reasonable OER current in the dark (**Figure 2 a**), with an onset below 1.6 V vs RHE. Upon illumination with red (630 nm) or green (520 nm) light, negligible change in current is observed during cyclic voltammetry (**Figure 2 a**). With 12 mW blue (460 nm) light illumination, minimal photocurrent is observed, in line with previous reports for LFO thin films illuminated at shorter wavelengths.²¹

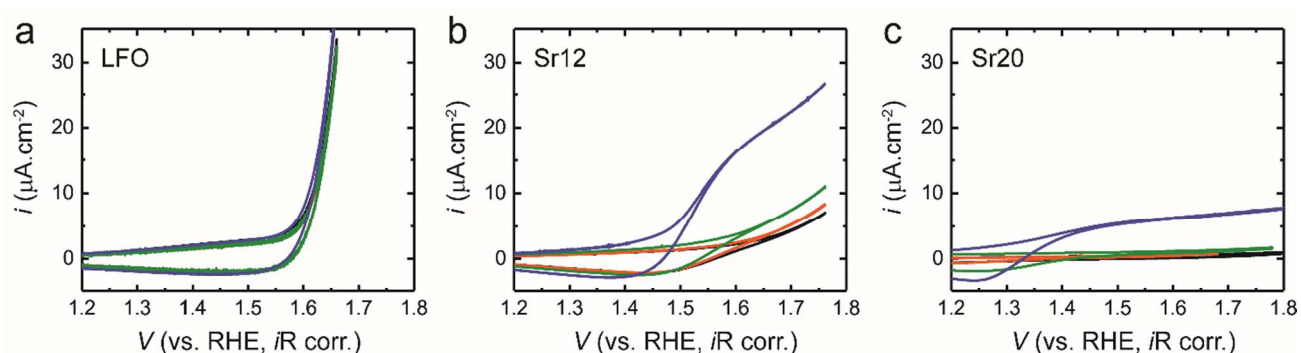


Fig 2. Cyclic voltammetry at 10 mV/s for (a) LFO (b) Sr12 and (c) LSF20 in O₂ saturated 0.1 M KOH. Curve colors correspond to the illumination wavelength: dark (black), red (630 nm, 10 mW), green (520 nm, 10 mW), and blue (460 nm, 12 mW).

With Sr incorporation, the OER current in dark decreases (**Figure 2 b, c**). This is in contrast to studies of particles supported on carbon or pressed into a disk,^{19, 37} and is likely impacted by the junction between the Nb:STO support and LSFO.³⁸ However, the band alignment of LFO/Nb:STO²¹ and Sr12/Nb:STO²⁸ has been previously measured by XPS, yielding similar valence band offsets ~2 eV. We thus expect the PEC activity trends to be characteristic of the LSFO/electrolyte interface, which is further confirmed by growing a 25 nm LFO buffer layer under a 5 nm Sr12 film, resulting in comparable performance (**Figure S5**). For

Sr12 and Sr20, only a small change in current is observed for red illumination, but a noticeable photovoltage and photocurrent are observed with green illumination, increasing further with blue (Figure 2 b, c) and exhibiting power-dependent photocurrent by CV (Figure S6), constant potential holding, or shuttering the light source during a potentiostatic hold at 1.65 V vs. RHE (Figure 3). As the Sr content increases, the difference between the onset voltage in dark and under illumination increases, being >0.5 V for Sr20. Although Sr12 has a lower difference in onset voltage of ~0.2 V, it exhibits a higher photocurrent.

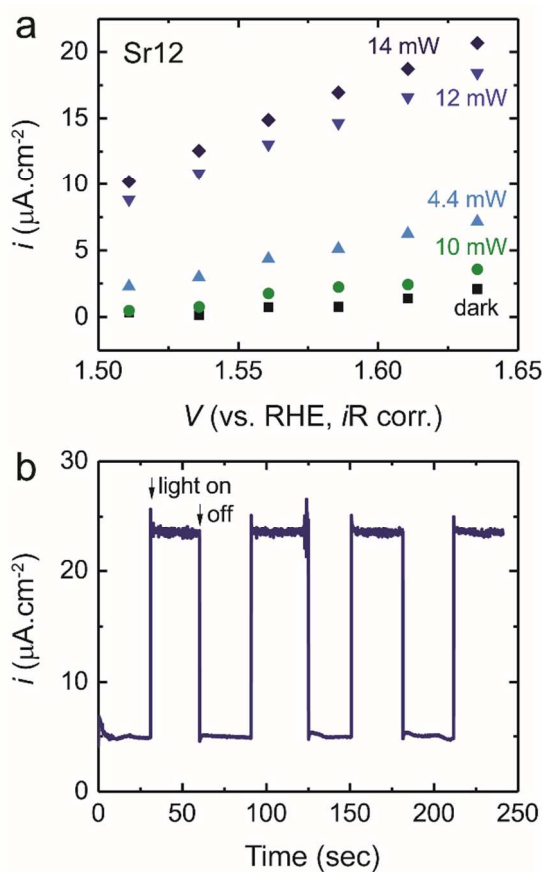


Fig 3. Illumination-dependent current density for Sr12 in O₂ saturated 0.1 M KOH. (a) Extracted steady-state current density from one minute of constant potential holding under the following conditions: in the dark (black), with 10 mW 520 nm illumination (green), or 460 nm illumination

at 4.4 mW (light blue), 12 mW (medium blue) and 14 mW (dark blue). The performance is comparable to that from cycling at 10 mV/s. (b) Slow shuttering of a 14 mW blue illumination, holding the applied potential at 1.65 V vs. RHE.

To better understand the limiting factors in photocurrent, we changed the thickness of the Sr12 film. For a heterostructure containing a thin 5 nm layer of Sr12 on top of a 25 nm layer of LFO (**Figure S5**), the current in dark and under illumination is nearly identical to that of the 30 nm Sr12 film, suggesting that photogenerated holes can only be collected from the top few nm of the film. In addition, this suggests that the lower photocurrent for Sr20 may arise from a shorter hole collection length due to the increase in carrier density from Sr substitution. Given the low hole mobility in transition metal oxides, this finding suggests that like most materials,⁸ LSFO photoelectrodes would benefit notably from nanostructuring. The photocurrent is low as expected for a reflective, planar surface, but initial measurements show it can readily be increased through combination with an electrodeposited NiOOH co-catalyst (**Figure S7**) of interest for further study. The discussion here is limited to the study of the LSFO/electrolyte interface for fundamental understanding.

To probe the electronic structure of the LSFO surface and the origin of the shifting photovoltage for OER, we employ a fast redox shuttle $[\text{Fe}(\text{CN})_6]^{3-/4-}$, “FeCN,” with comparable redox potential in the pH 13 electrolyte (**Figure 4, Figure S8**). Studies of Fe_2O_3 in contact with FeCN have established the outer sphere nature of the reaction and that the surface-hole collection efficiency is essentially unity.³⁹ The difference in overpotential required to initiate water oxidation compared to the fast redox shuttle can then be attributed to differences in the surface-hole collection efficiency.⁶ Compared to driving the OER under 460 nm blue light illumination

in KOH only, the onset of FeCN oxidation occurs 0.3 to 0.4 V lower in energies for Sr12 and Sr20, respectively (**Figure 4**). Thus, while the LSFO surface can supply photoexcited holes at these low potentials, they cannot be efficiently collected to drive water oxidation and are instead ‘trapped’ by states at the surface.

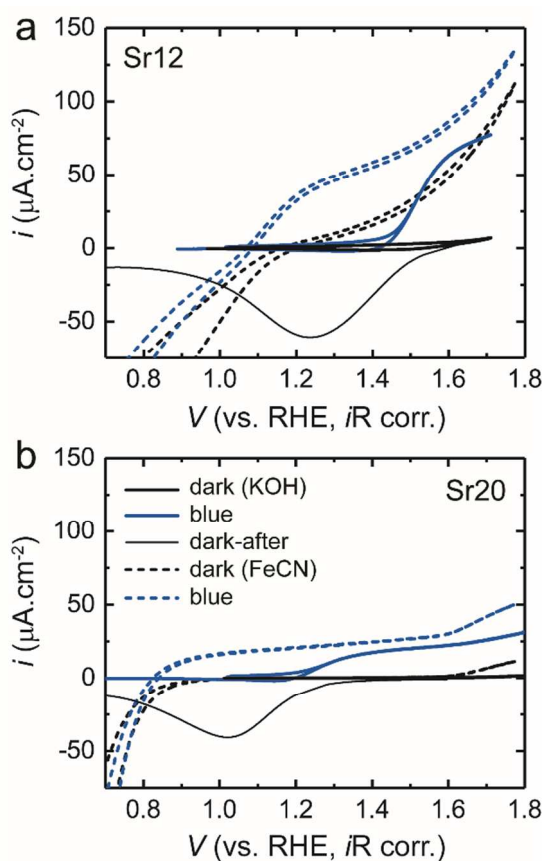


Fig 4. Measurements of Sr12 (a) and Sr20 (b) in 0.1 M KOH at 10 mV/s in the dark (black, thick solid) and with ~ 24 mW 460 nm illumination (blue solid) driving the OER, compared with adding 10 mM of an FeCN hole scavenger (dashed). In FeCN, the photovoltage increases; the shift between the KOH only and FeCN+KOH illuminated curves corresponds with the surface states (thin black line), probed in KOH at 200 mV/s after >2 minutes illumination at 1.65 V.

The surface trapping of holes can be considered as the photooxidation of a chemical species on the surface, and surface recombination as the reduction of that oxidized surface species. When a positive potential is applied under illumination (in KOH only), holes accumulate on the surface. Subsequent scanning of the potentially negatively by CV in the dark to measure the cathodic current then reduces these surface states,⁶ which we observe coincides with the difference in onset potential between FeCN and the OER (**Figure 4**). The peak in cathodic current is not observed on subsequent cycles (**Figure 5**), consistent with the reduction of surface trapped holes as the potential is scanned negative on the first cycle, illustrated by the shaded regions.

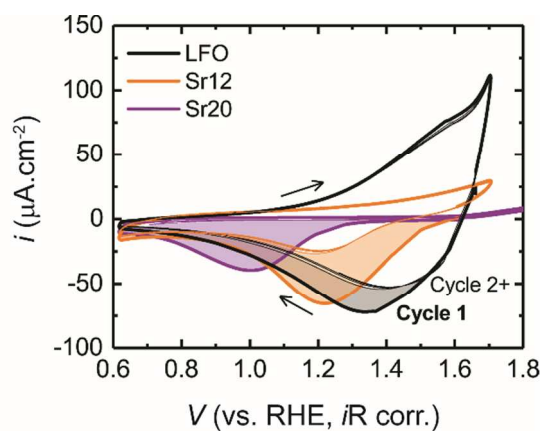


Fig 5. Comparison of surface states, probed in 0.1 M KOH at 200 mV/s after >2 minutes of ~24 mW 460 nm illumination at 1.65 V. The first sweep (cycling first toward lower potentials) is shown in bold, with subsequent cycles shown as a thin line. The difference between first and subsequent cycles (shaded) is indicative of the discharge of surface states filled during illumination at OER conditions.

The illuminated CVs in the electrolyte containing FeCN represent the potential-dependent fraction of photogenerated holes that reach the electrode surface, where they are

efficiently collected by the redox shuttle. Under water oxidation conditions, the flux of holes to the surface—a property of the same semiconductor electrode—remains the same, but steady-state photocurrent is not produced at low applied potentials. Holes are initially trapped at surface states (intermediates in the overall water oxidation reaction), and the remainder recombine. However we note that at high potentials, the photocurrent in FeCN is somewhat higher than in KOH only, which has been attributed to the extra potential needed to compensate for Fermi level pinning in the KOH only.⁶

Having established the presence of surface states on the LSFO films which must be oxidized prior to the onset of photovoltage for the OER, and that the potential at which these are observed changes with Sr content, we seek information regarding the chemical nature of these OER intermediates. Specifically, we characterize the surface chemistry of LSFO films in a humid and oxidizing environment using AP-XPS. For Fe₂O₃, many consider the first step of water oxidation to be the proton-coupled oxidation of surface hydroxide species.^{6, 40} A similar mechanism has been proposed for perovskite oxides.^{11, 17} Thus we probe the ability of LSFO films to form hydroxyls in equilibrium with water vapor.^{11, 41}

Given that Sr²⁺ substitution for La³⁺ is known to both oxidize Fe and lead to the incorporation of oxygen vacancies, we first explicitly probe the behavior of surface oxygen vacancies in a humid environment. Two Sr12 films were first cleaned by heating to 300 °C in 100 mTorr O₂ to remove adventitious carbon from air exposure during transport. One film was then heated in ultra-high vacuum to 600 °C in order to induce oxygen vacancies, and returned to 300 °C. This annealing step did not result in any change in the elemental ratio at the surface (**Figure S9**). The presence of oxygen vacancies is confirmed by the reduction in the low-energy pre-edge feature in XAS (**Figure S10**) that increases with Sr incorporation.

We probe the oxygen speciation of Sr12 as a function of H₂O pressure in a 300 °C isotherm, where the surface remains clean of carbon (**Figure 6**). In dry 100 mTorr O₂ or vacuum environments, the O 1s spectra is dominated by a peak at low relative binding energies (~529 eV relative to the Fermi level), characteristic of bulk oxygen.³⁰ In O₂, a doublet from the gas phase is present >9 eV above the bulk. For the as-prepared film measured in O₂ to prevent oxygen vacancy formation, a shoulder at 2.6 eV higher binding energies is present, found from depth profiling to be located at the surface (**Figure S11**). Studies of (001)-oriented LFO selectively terminated with the La- or Fe-containing layer show this “surface” feature is characteristic of undercoordinated oxygen adsorbates on the LaO termination and is not observed on the FeO₂ plane.⁴² This surface feature disappeared upon vacuum heat treatment for the annealed Sr12 film, indicating these adsorbates can be removed at high temperatures and do not return in vacuum at 300 °C. Upon the introduction of 10 mTorr of H₂O, a peak at 1.25 eV above the bulk increases as water dissociates on the surface to form hydroxyl species, where the intensity of this peak relative to the bulk peak is proportional to coverage (**Figure S9 c**). An increase in the “surface” feature with water exposure is consistent with previous studies of La_(1-x)Sr_xCrO₃,⁴³ La_(1-x)Sr_xMnO₃,⁴² and LaO-terminated LFO,⁴² indicating these oxygen species located on the AO plane protonate in humid conditions. The annealed Sr12 surface exhibits a notably higher amount of OH compared to the as-prepared surface, illustrating that oxygen vacancies are filled by the dissociation of water, as observed for other oxides such as TiO₂.⁴⁴ As the humidity increases, however, the amount of OH appears to saturate, indicating that all surface oxygen vacancies are filled in contact with water. Both as-prepared and annealed Sr12 exhibit a similar oxygen speciation both in a mixture of 100 mTorr O₂ + 100 mTorr H₂O and pure 100 mTorr H₂O (**Figure S12**); this similarity is also reflected in the valence band (**Figure S13**).

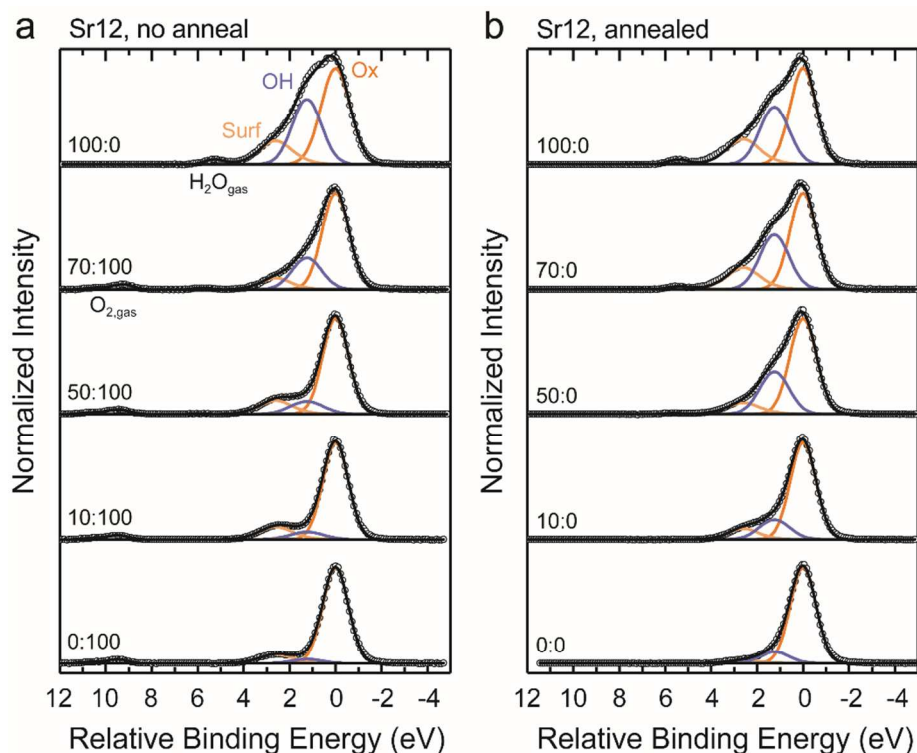


Fig 6. AP-XPS of Sr12 as a function of water atmosphere at 300 °C (a) not annealed, in a background of 100 mTorr O₂ and (b) annealed in UHV to induce oxygen vacancies. The O 1s spectra, Shirley background subtracted and normalized to the bulk “Ox” (dark orange) intensity, are probed at an incident photon energy of 690 eV, and the pressure is given as $p(\text{H}_2\text{O}):p(\text{O}_2)$ in mTorr. Oxygen vacancies promote the dissociation of water to form OH species (blue) at low humidity but the extent of hydroxylation is comparable at high humidity.

We next consider the influence of Sr incorporation on the oxygen speciation in a humid environment, comparing Sr12 (**Figure 6 a**) and Sr20 (**Figure S14**) in a water isotherm at 300 °C in a background of 100 mTorr O₂ to avoid oxygen vacancy formation during measurements. Probing surface speciation at moderate temperatures enables comparison of hydroxylation without interference from oxygen-containing carbon species, where a range of relative humidity is accessed by changing water partial pressure. We note the LSFO crystal structure⁴⁵ and oxygen

content^{46, 47} do not change notably from 300 °C to room temperature. The ratio of the OH or surface component to the bulk lattice feature in the O 1s (**Figure 7**) is proportional to coverage. For intermediate H₂O pressures, Sr20 exhibits a notably higher amount of OH compared to Sr12, although the ratio of OH/bulk is more similar at high relative humidity. This indicates that for a given relative humidity (or reducing potential), the Sr20 surface is characterized with more OH sites, consistent with the presence of surface intermediate states at lower potentials on the RHE scale by cyclic voltammetry (**Figure 5**). The formation of OH species at Fe sites oxidized by Sr incorporation occurs in parallel with a reduction in the low-energy feature of the O K-edge pre-peak in H₂O (**Figure S15**). This indicates that Fe is reduced at the surface by OH formation, previously observed on Fe₃O₄.⁴⁸ The Sr20 surface also exhibits a higher amount of “surface” oxygen species than Sr12. The near-surface stoichiometry of the LSFO films shows the expected trends in composition (**Figure S16**), however there could be a higher amount of AO termination of the Sr20 or a higher affinity of SrO (vs LaO) planes for this “surface” chemical speciation.

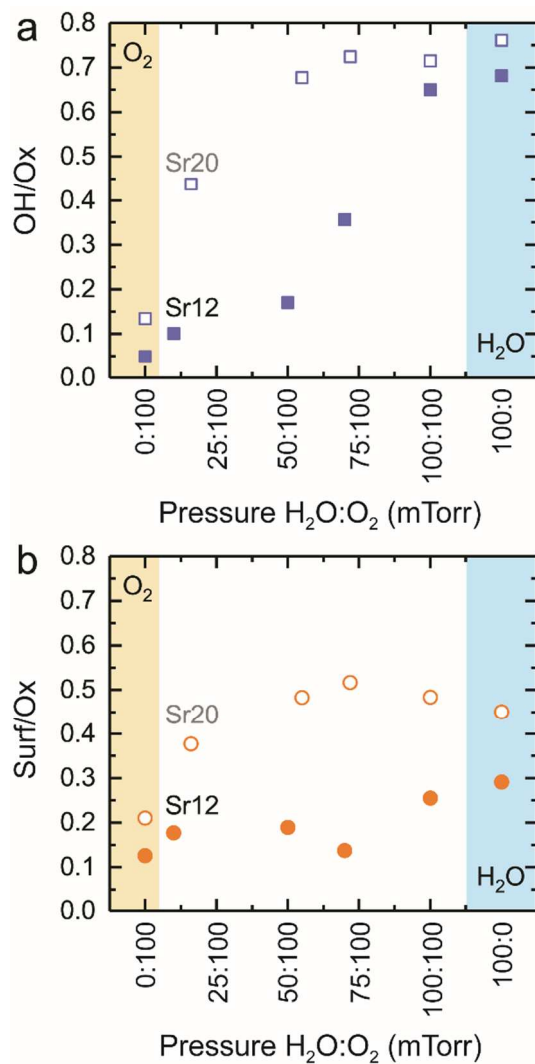
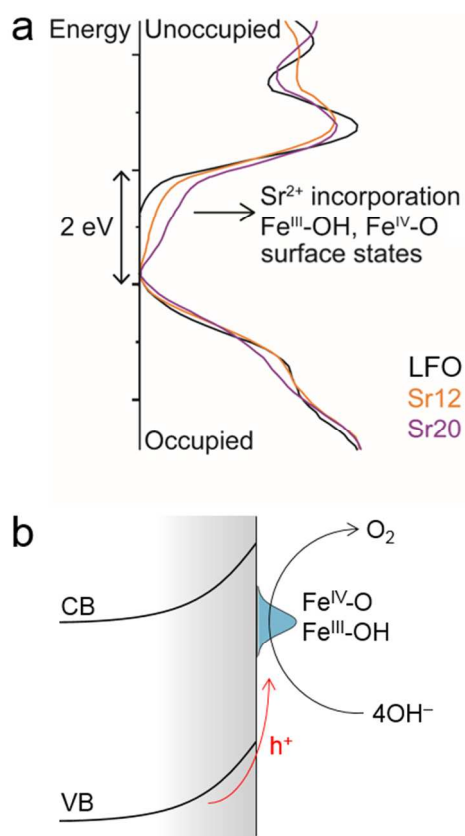


Fig 7. Comparison of surface speciation on Sr12 and Sr20 at 300 °C, obtained from AP-XPS of the O 1s probed at 690 eV. The pressure of H₂O: O₂ in mTorr is given, starting at 100 mTorr O₂ (yellow bar) and adding varying water atmospheres up to 100 mTorr H₂O, and then in 100 mTorr H₂O without O₂ (blue bar). Sr substitution for La promotes (a) the formation of hydroxyls, where the coverage is proportional to the ratio of the OH component to the bulk Ox feature, and (b) the surface oxygen component, characteristic of (hydro)peroxo species at the A-site.⁴²

Considering the implications of Sr²⁺ incorporation in LSFO, the resultant unoccupied states (**Scheme 1a**) are readily filled upon interaction with water, leading to hydroxyl and

protonated “surface” species (or OOH) groups. The formation of these species occurs more readily on Sr20 than Sr12 in a humid environment, indicating their stronger binding. This is consistent with the more reducing potentials of surface states observed upon cycling in the dark after oxidative holding under illumination. Comparing the PEC behavior of these films in aqueous KOH electrolyte to that containing the fast redox shuttle FeCN, the lower onset potential with the efficient hole collector—below the potential of the surface states—indicates that water oxidation occurs by first oxidizing these Fe^{III}-OH surface states to Fe^{IV}-O containing species (**Scheme 1b**).



Scheme 1. Illustration of the changes in electronic structure for LSFO, how this dictates surface speciation, and the implications for PEC. (a) A schematic of the density of states (2 eV for scale) from XAS and XPS measurements shows that Sr incorporation leads to unoccupied states

(nominally Fe^{IV}), which are probed at the surface using AP-XPS where they hydroxylate ($\text{Fe}^{\text{III}}\text{-OH}$) upon interaction with H_2O . (b) Under illumination, the OER proceeds by oxidizing LSFO surface states, such as $\text{Fe}^{\text{III}}\text{-OH}$ to $\text{Fe}^{\text{IV}}\text{-O}$, prior to the onset of steady state photocurrent. In contrast, FeCN efficiently collects holes (h^+) and does not proceed via these states, leading to a lower onset potential.

Conclusion:

Together, these investigations of the surface chemistry, electronic structure, and PEC performance of LSFO films bring new understanding to the role of A-site aliovalent substitution in a complex oxide where the B-site is active for OER. Although Sr^{2+} substitution for La^{3+} can induce oxygen vacancies, these facilitate H_2O dissociation and are thus filled by surface OH groups as revealed by AP-XPS. The influence of oxygen vacancies on bulk oxide absorption properties merits further study. Sr incorporation additionally promotes Fe oxidation, observed by changes in the O K-edge spectra in an oxidizing environment. This decreases the optical band gap, and results in an increased photovoltage in PEC measurements of the OER. Measurements with the efficient hole collector FeCN indicate an even lower onset to photoabsorption, with the higher voltage onset of OER arising from the need to oxidize surface states. We find these surface states are at a lower potential on the RHE scale with Sr incorporation, indicating that their oxidation is promoted (occurring at less oxidizing potentials) in tandem with the lower onset of water oxidation. To better understand the chemical identity of these surface states, we consider the surface speciation in an aqueous environment using AP-XPS. The oxidation of $\text{Fe}^{\text{III}}\text{-OH}$ species to $\text{Fe}^{\text{IV}}\text{-O}$ has been suggested as the first step in the OER reaction mechanism for other iron oxides, and we probe the affinity of LSFO species for OH explicitly with this

technique. At a given H₂O pressure, more OH species are observed for higher Sr concentrations. Their formation in a reducing environment is consistent with the observation of surface states at lower potentials in cyclic voltammetry. Together, these findings indicated that the increase in OER photovoltage with Sr substitution in LSFO can be attributed to the promotion of Fe oxidation.

Acknowledgements:

The thin film growth and structural characterization work was supported by the U.S. Department of Energy (DOE), Office of Science, Division of Materials Sciences and Engineering under award #10122. PEC and AP-XPS measurements performed by K.A.S. were supported by the Linus Pauling Distinguished Post-doctoral Fellowship at Pacific Northwest National Laboratory (PNNL LDRD 69319). Y.D. acknowledges the support by U.S. DOE, Office of Science, Office of Basic Energy Sciences, Early Career Research Program under Award No. 68278 for traveling to ALS and participating in the AP-XPS measurements. A portion of the work was performed at the W. R. Wiley Environmental Molecular Sciences Laboratory, a DOE User Facility sponsored by the Office of Biological and Environmental Research. PNNL is a multi-program national laboratory operated for DOE by Battelle. This research used resources of the Advanced Light Source, which is a DOE Office of Science User Facility under contract no. DE-AC02-05CH11231.

References:

1. M. G. Walter, E. L. Warren, J. R. McKone, S. W. Boettcher, Q. Mi, E. A. Santori and N. S. Lewis, *Chemical Reviews*, 2010, **110**, 6446-6473.

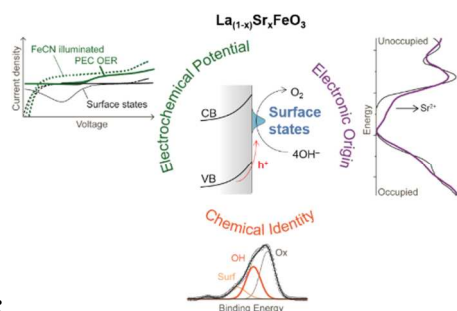
2. A. Fujishima and K. Honda, *Nature*, 1972, **238**, 37.
3. K. Sivula and R. van de Krol, *Nature Reviews Materials*, 2016, **1**, 15010.
4. B. Iandolo, B. Wickman, I. Zoric and A. Hellman, *Journal of Materials Chemistry A*, 2015, **3**, 16896-16912.
5. O. Zandi and T. W. Hamann, *Nature Chemistry*, 2016, **8**, 778.
6. B. Klahr, S. Gimenez, F. Fabregat-Santiago, J. Bisquert and T. W. Hamann, *Energy & Environmental Science*, 2012, **5**, 7626-7636.
7. A. Shavorskiy, X. Ye, O. Karslıoğlu, A. D. Poletayev, M. Hartl, I. Zegkinoglou, L. Trotochaud, S. Nemšák, C. M. Schneider, E. J. Crumlin, S. Axnanda, Z. Liu, P. N. Ross, W. Chueh and H. Bluhm, *The Journal of Physical Chemistry Letters*, 2017, **8**, 5579-5586.
8. R. Van De Krol, in *Photoelectrochemical hydrogen production*, Springer, 2012, pp. 13-67.
9. M. Rioult, H. Magnan, D. Stanescu and A. Barbier, *The Journal of Physical Chemistry C*, 2014, **118**, 3007-3014.
10. H. Magnan, D. Stanescu, M. Rioult, E. Fonda and A. Barbier, *Applied Physics Letters*, 2012, **101**, 133908.
11. K. A. Stoerzinger, W. T. Hong, E. J. Crumlin, H. Bluhm and Y. Shao-Horn, *Accounts of Chemical Research*, 2015, **48**, 2976-2983.
12. S. N. Tijare, M. V. Joshi, P. S. Padole, P. A. Mangrulkar, S. S. Rayalu and N. K. Labhsetwar, *International Journal of Hydrogen Energy*, 2012, **37**, 10451-10456.
13. K. M. Parida, K. H. Reddy, S. Martha, D. P. Das and N. Biswal, *International Journal of Hydrogen Energy*, 2010, **35**, 12161-12168.
14. K. Peng, L. Fu, H. Yang and J. Ouyang, *Scientific Reports*, 2016, **6**, 19723.

15. M. D. Scafetta, A. M. Cordi, J. M. Rondinelli and S. J. May, *Journal of Physics: Condensed Matter*, 2014, **26**, 505502.
16. W. T. Hong, K. A. Stoerzinger, B. Moritz, T. P. Devereaux, W. Yang and Y. Shao-Horn, *The Journal of Physical Chemistry C*, 2015, **119**, 2063-2072.
17. J. Suntivich, K. J. May, H. A. Gasteiger, J. B. Goodenough and Y. Shao-Horn, *Science*, 2011, **334**, 1383-1385.
18. B. Han, A. Grimaud, L. Giordano, W. T. Hong, O. Diaz-Morales, L. Yueh-Lin, J. Hwang, N. Charles, K. A. Stoerzinger, W. Yang, M. T. M. Koper and Y. Shao-Horn, *The Journal of Physical Chemistry C*, 2018, **122**, 8445-8454.
19. A. Wattiaux, J. C. Grenier, M. Pouchard and P. Hagenmuller, *Journal of The Electrochemical Society*, 1987, **134**, 1714-1718.
20. G. S. Pawar and A. A. Tahir, *Scientific Reports*, 2018, **8**, 3501.
21. K. J. May, D. P. Fenning, T. Ming, W. T. Hong, D. Lee, K. A. Stoerzinger, M. D. Biegalski, A. M. Kolpak and Y. Shao-Horn, *The Journal of Physical Chemistry Letters*, 2015, **6**, 977-985.
22. Z. Zhu, H. Peelaers and C. G. Van de Walle, *Journal of Materials Chemistry A*, 2017, **5**, 15367-15379.
23. Q. Peng, B. Shan, Y. Wen and R. Chen, *International Journal of Hydrogen Energy*, 2015, **40**, 15423-15431.
24. I. Natali Sora, F. Fontana, R. Passalacqua, C. Ampelli, S. Perathoner, G. Centi, F. Parrino and L. Palmisano, *Electrochimica Acta*, 2013, **109**, 710-715.
25. M. D. Scafetta, Y. J. Xie, M. Torres, J. E. Spanier and S. J. May, *Applied Physics Letters*, 2013, **102**, 081904.

26. B. M. Klahr, A. B. F. Martinson and T. W. Hamann, *Langmuir*, 2011, **27**, 461-468.
27. L. Qiao, T. C. Droubay, T. Varga, M. E. Bowden, V. Shutthanandan, Z. Zhu, T. C. Kaspar and S. A. Chambers, *Physical Review B*, 2011, **83**, 085408.
28. L. Wang, Y. Du, L. Chang, K. A. Stoerzinger, M. E. Bowden, J. Wang and S. A. Chambers, *Applied Physics Letters*, 2018, **112**, 261601.
29. M. E. Grass, P. G. Karlsson, F. Aksoy, M. Lundqvist, B. Wannberg, B. S. Mun, Z. Hussain and Z. Liu, *Review of Scientific Instruments*, 2010, **81**, 053106.
30. K. A. Stoerzinger, W. T. Hong, E. J. Crumlin, H. Bluhm, M. D. Biegalski and Y. Shao-Horn, *The Journal of Physical Chemistry C*, 2014, **118**, 19733-19741.
31. Y. J. Xie, M. D. Scafetta, E. J. Moon, A. L. Krick, R. J. Sichel-Tissot and S. J. May, *Applied Physics Letters*, 2014, **105**, 062110.
32. S. Y. Smolin, M. D. Scafetta, A. K. Choquette, M. Y. Sfeir, J. B. Baxter and S. J. May, *Chemistry of Materials*, 2016, **28**, 97-105.
33. D. N. Mueller, M. L. Machala, H. Bluhm and W. C. Chueh, *Nature Communications*, 2015, **6**, 6097.
34. W. H. Jung and E. Iguchi, *Journal of Physics: Condensed Matter*, 1995, **7**, 1215.
35. M. Abbate, F. M. F. de Groot, J. C. Fuggle, A. Fujimori, O. Strebel, F. Lopez, M. Domke, G. Kaindl, G. A. Sawatzky, M. Takano, Y. Takeda, H. Eisaki and S. Uchida, *Physical Review B*, 1992, **46**, 4511-4519.
36. H. Wadati, D. Kobayashi, H. Kumigashira, K. Okazaki, T. Mizokawa, A. Fujimori, K. Horiba, M. Oshima, N. Hamada, M. Lippmaa, M. Kawasaki and H. Koinuma, *Physical Review B*, 2005, **71**, 035108.

37. S. She, J. Yu, W. Tang, Y. Zhu, Y. Chen, J. Sunarso, W. Zhou and Z. Shao, *ACS Applied Materials & Interfaces*, 2018, **10**, 11715-11721.
38. A. Sawa, A. Yamamoto, H. Yamada, T. Fujii, M. Kawasaki, J. Matsuno and Y. Tokura, *Applied Physics Letters*, 2007, **90**, 252102.
39. B. M. Klahr and T. W. Hamann, *The Journal of Physical Chemistry C*, 2011, **115**, 8393-8399.
40. A. Hellman and R. G. S. Pala, *The Journal of Physical Chemistry C*, 2011, **115**, 12901-12907.
41. K. A. Stoerzinger, W. T. Hong, G. Azimi, L. Giordano, Y.-L. Lee, E. J. Crumlin, M. D. Biegalski, H. Bluhm, K. K. Varanasi and Y. Shao-Horn, *The Journal of Physical Chemistry C*, 2015, **119**, 18504-18512.
42. K. A. Stoerzinger, R. Comes, S. R. Spurgeon, S. Thevuthasan, K. Ihm, E. J. Crumlin and S. A. Chambers, *The Journal of Physical Chemistry Letters*, 2017, **8**, 1038-1043.
43. S. K. A., D. Yingge, I. Kyuwook, Z. K. H. L., C. Jun, D. J. Trey, F. R. T., H. G. S., C. E. J. and C. S. A., *Advanced Materials Interfaces*, 2018, **5**, 1701363.
44. G. Ketteler, S. Yamamoto, H. Bluhm, K. Andersson, D. E. Starr, D. F. Ogletree, H. Ogasawara, A. Nilsson and M. Salmeron, *The Journal of Physical Chemistry C*, 2007, **111**, 8278-8282.
45. F. Anita, M. Mohan, W. Ivar, W. Kjell, E. Mari-Ann and G. Tor, *Journal of the American Ceramic Society*, 2004, **87**, 1952-1958.
46. D. D. Taylor, N. J. Schreiber, B. D. Levitas, W. Xu, P. S. Whitfield and E. E. Rodriguez, *Chemistry of Materials*, 2016, **28**, 3951-3960.

47. J. A. Bahteeva, I. A. Leonidov, M. V. Patrakeev, E. B. Mitberg, V. L. Kozhevnikov and K. R. Poeppelmeier, *Journal of Solid State Electrochemistry*, 2004, **8**, 578-584.
48. K. A. Stoerzinger, C. I. Pearce, T. C. Droubay, V. Shutthanandan, A. Shavorskiy, H. Bluhm and K. M. Rosso, *The Journal of Physical Chemistry C*, 2017, **121**, 19288-19295.



TOC: